L2 Earth Atmosphere Observatory: Formation Guidance, Metrology and Control Synthesis

A. Behçet Açıkmeşe, Edward Mettler, William G. Breckenridge, Steven A. Macenka, and Eldred F. Tubbs

Jet Propulsion Laboratory
California Institute of Technology
Pasadena, CA 91109

July 26, 2004

Abstract

The Earth Observatory Formation at L2, a Lagrange libration point, is a unique large aperture (25 m diameter) space telescope concept that will improve the knowledge and understanding of dynamic, chemical and radiative mechanisms that cause changes in the atmosphere, and can lead to the development of models and techniques to predict short and long-term climate changes. The results of this concept definition study show that the telescope concept is feasible, and can have technology readiness in the 2020 time frame. Further advanced development in several subsystems is needed, such as higher efficiency Xenon ion thrusters with throttling, and optical quality large membrane mirror with active shape control.

It presents an analysis and solution of guidance, sensing, control, and propulsion problems for a formation of two spacecraft on the Sun-Earth line in the neighborhood of the Sun-Earth L2 point, that observes Earth's atmosphere during continuous solar occultation by the Earth.

A system architecture is described for the observatory, and its components that include unique mission specific metrology. The formation must follow a powered trajectory with strictly limited fuel use to observe solar occultation. A configuration of ion thrusters and reaction wheels for translation and attitude control is designed along with algorithms for orbit following and formation control. Simulation results of the orbital and formation dynamics are presented that verify performance of the control systems.

1 Introduction

In this paper, we describe the overall system architecture of a revolutionary Earth Atmosphere Observatory Formation concept, and analyze the sensing, guidance, actuation, and precision control methods for the formation of two spacecraft in orbit in the neighborhood of the Sun-Earth L2 (Lagrange) point, and station-keeping on the Sun-Earth line at approximately 1.5 million kilometers from the Earth, to

observe the Earth in continuous occultation of the sun. This formation is composed of a Secondary Telescope spacecraft, pointed at a 25-meter membrane mirror on a Primary Aperture spacecraft 125-meters distant on-axis in formation flying precision alignment, that scans the focused image of the illuminated atmosphere of the Earth reflected from the large mirror (see Figure 1).

The sensors in this mission includes standard sensors such as sun sensors, and star trackers, and also some mission specific sensors, such as formation RF (radio frequency) and optical metrology, Earth-Sun sensor, large mirror surface figure-sensor, and center of curvature sensor. The detailed descriptions of these mission specific sensors are provided in this paper.

The Sun-Earth L2 point is an actual equilibrium point of the two body problem described by Sun and Earth. The only other significant gravitational force is due to the Moon so that an actual equilibrium point is not at Sun-Earth L2, but it is at the very close proximity of the Sun-Barycenter (barycenter of Earth-Moon) L2 point. Our objective is for the observatory to track a point on the Sun-Earth line in the neighborhood of the Sun-Earth L2 point, with a minimum penalty of fuel use.

The choice of the reference orbit determines the forces acting on the spacecraft during operations, and the magnitude of the thrusting needed to counteract gravitational forces due to Sun, Earth, and Moon, and disturbance forces due to solar pressure. The analysis of the reference orbit in terms of these forces lead to the design of a specific an actuator configuration and sizing. The gravitational forces should be counterbalanced in order to track the reference orbit, and the differential solar forces should be counteracted in order to keep a highly accurate formation control. Therefore, we choose two sets types of thrusters, one set has thrusters with 45 mN maximum thrust and it provides orbital control forces, whereas the second set has thrusters with maximum thrust of 5 mN that provide the formation control forces.

There are three basic control actions that are computed by the control algorithm: (i) Orbit following control, (ii) Formation control, and (iii) Attitude control. We presented a multi-input-multi-output (MIMO) PID (proportional-integral-derivative) control algorithm for each. Since the measurements errors in orbital quantities are much larger than the formation quantities (many orders of magnitude larger), the bandwidth of closed loop orbit following is much smaller than the bandwidth of closed loop formation dynamics.

One of the major challenges in this mission is the shape control of the large membrane mirror on Primary Aperture spacecraft. This involves the determination of the shape from sensor measurements, modelling of the membrane mirror, development of the actuation system, and the algorithms that compute the control forces to be applied on the mirror. We propose a quasi-static sensing and control scheme based on modal description of the shape, and propose an actuator system delivering the necessary forcing.

Our observatory concept definition identifies the key technology advances required of current electric propulsion technology, as well as for optical metrology sensors, and ultra-lightweight actively controlled membrane mirror technology that will enable this mission. With these feasible developments over the current and next decade, we will be able to realize the benefits of an Earth Atmosphere Observatory at L2.

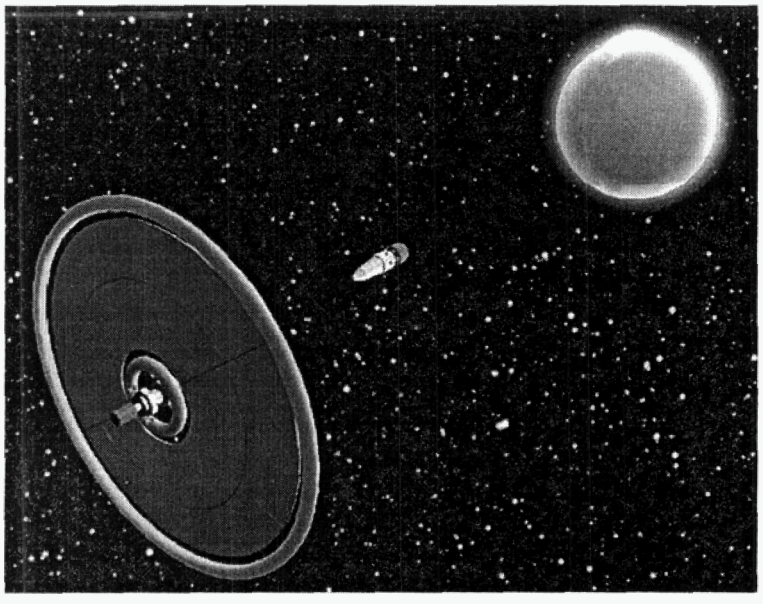

Figure 1: Atmosphere Observatory Formation at L2 Viewing Solar Occultation by Earth

2 System Architecture

The proposed observatory at L2 is a formation of two spacecraft, *science* (S/C-S) and *large aperture* (S/C-A) spacecraft. S/C-S is located between S/C-A and Earth, and it is equipped with a science telescope pointing at a large mirror on S/C-A, attached to a bus. The bus module of both spacecraft has the engineering equipment: sensors, reaction wheels, thrusters, communication equipment etc. The image reflected by the membrane mirror is scanned by this telescope that has a corrector mirror to correct for the spherical abberations caused by the membrane mirror.

S/C-A is 125 meters away from S/C-S on Sun-Earth line. It has an $f/5$ spherical membrane mirror, with a 25 meter outer and 7 meter inner diameter that is supported by inflatable torus in the outer and inner diameters. There is an engineering bus at the center of the large mirror that contains guidance and control hardware. The Primary Aperture is 25 m diameter to satisfy the science driven 1 km resolution at Earth over a broadband spectrum, i.e. diffraction limit of 67 micro-radian at 10.5 microns. Then, the theoretical size requirement for this large aperture is 19 m with added margin for membrane boundary conditions. The Earth and Sun are extended objects viewed from L2, and they require a *spherical aperture* system or *Schmidt telescope* concept to handle *wide angle and high resolution*.

First a spherical mirror with a focal ratio of $f/10$ was considered. This implies a focal length of 250 m, and a center of curvature of 500 m. However, the desired f/10 optics creates an excessively large (2.5 m) Solar Light Annulus image at the Primary focal plane. So, the optical system design is constrained to a practical $f/5$ with annulus size of 1.25 m, in order to keep the Science Telescope optics and S/C size/mass within realistic limits. The $f/5$ telescope assembly mass is less than 10% of the mass of the $f/10$ telescope. However, this significant reduction in mass comes with some other

design challenges, and some of those are:

- Faster $f/5$ primary mirror is more prone to spherical aberration and less depth of field tolerance.
- Smaller size relay and corrector elements required for $f/5$ mirror are more difficult to design (Lagrange invariant) for required performance.
- Ratio of 25 m to 1 m pupil magnification increases distortion.
- Greater number of optical elements required reduces broadband energy throughput of optical train.
- Required Corrector Aspheric is more complex to design and fabricate.
- A *fast steering mirror* is required for beam stabilization.

The main science requirements are:

- Earth atmospheric observation from the neighborhood of Earth-Sun point.
- Scan the Earth atmosphere with 100 km surface (latitude, longitude 90°).
- Sample the atmosphere with 1 km vertical resolution.
- Navigate in 200 km radius tube around Sun-Earth line to maintain Sun annulus around Earth.
- Large aperture telescope for a resolution of less than 0.67 μrad for observations at wavelengths from 0.28 μm to 10.5 μm.
- Angular jitter less than 0.13 arc-sec (0.63 μrad) (peak-peak) for frequencies larger than 100 Hz.
- Knowledge of control jitter to less than 0.2 km for lower frequencies.

The science requirements above impose specific engineering requirements on the system. Some of these requirements, and the error allocations are summarized below:

- Lateral position from the Sun-Earth line $\leq 200km$.
- Allowable Earth range variation $\rightarrow \pm$ 5000 km.
- Earth relative pointing: Communication using HGA (high gain antenna) $\rightarrow \pm$ 436 μrad.
- Image position error perpendicular to LOS (line of sight) in order to fit within a 5 cm telescope entrance aperture $\rightarrow \pm$2 cm.

3 Sensors

The following sensors are used in this mission:

1. Formation RF metrology.
2. Optical Metrology.
3. Earth-Sun sensor.
4. Surface-figure sensor.
5. Center-of-curvature sensor.
6. Standard spacecraft sensor suite, sun sensors, and star trackers.

The sensors 1-5 in this list are mission specific sensors, where as item 6 describes the standard set of sensors. In this section, we discuss the mission specific sensors, items 1-5.

3.1 Formation RF Metrology

It provides GPS-like range and phase measurements between transmitter and receiver, which are triangulated to get relative position and attitude of S/C-A for acquisition and coarse formation control, Figure 2. This metrology suite will use JPL's existing "TurboRogue" transceivers, which are readily adaptable to variable baselines from 100m to a 1 km separation. The current capability for measurement precision ($1-\sigma$ values) are :

- 1 cm relative range.
- 1 arc-min relative orientation.
- 0.1 mm/sec relative velocity.

The sensor depends for its operation on synchronized precision clocks at each station. A pseudo-random sequence is generated by algorithm from each clock. The distance is determined by comparing the phase of the received sequence with that of the locally generated one. The 6 distances measured by the system constitute a virtual truss that uniquely locates each spacecraft with respect to the other.

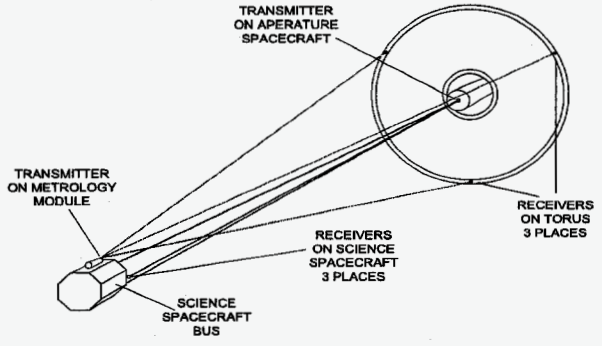

Figure 2: Formation RF Metrology

3.2 Formation Optical Metrology

The optical metrology performs two functions by operating in two different modes. In the first mode, optical metrology uses laser that is reflected back from several (3-4) retro-reflectors placed on outer and inner toroidal circumferences of the mirror, and one in the center of the mirror, to precisely measure relative formation range and bearing, attitude, and zeroth order mirror shape (tip, tilt, and piston) for fine formation control and Earth image location prediction. The current capability for measurement precision ($1-\sigma$ values) are:

- 1 micro-m relative range.
- 10 micro-rad relative bearing.

The technology is the same as that of the Surface-Figure Sensor but the returned signal is higher from more efficient retro-reflectors that are not constrained to conform to the surface of the primary mirror. This allows these measurements to be made more rapidly then what is needed for precise control of the formation.

3.3 Earth-Sun Sensor

This sensor images Earth and Sun to find points on the limbs, and determine

- Relative Earth direction,
- Position offset from Earth-Sun line,
- Course Earth range.

A *Maksutov telescope* of 10 cm aperture images the Earth and Sun on an array detector. The field of view is $1° \times 1°$, and the detector is 4096×4096 pixels, Figure 3. The telescope is preceded by heat-rejection and narrow-band filters. The detector output is processed to yield the centroid of both the Earth and Sun images in all conditions of alignment.

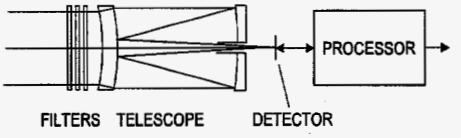

Figure 3: Earth-Sun Sensor

3.4 Surface-Figure Sensor

The Surface-Figure Sensor uses a new interferometric technology: Modulation Sideband Technology for Absolute Ranging (MSTAR) together with precision angular measurement to determine the three-dimensional location of retroreflective targets on the surface of the primary mirror. The MSTAR system has been described by Lay et al. [17] and will only be summarized here. Referring to the diagram, Figure 4, we see that the laser light is divided into two paths to provide illumination for the two arms of the interferometer. Each arm contains a frequency shifter and a phase modulator. The frequencies in each arm are slightly different and are chosen so that when the sidebands are mixed on the photodetector array the resulting frequencies are in the kilohertz range, e.g. 50 kHz and 130 kHz. These frequencies are in the range that can be processed by the active-pixel detector. This simplifies the signal processing but allows the use of fast phase modulators to resolve the ambiguity inherent in standard heterodyne interferometers, thus creating an absolute distance measurement. By using fast modulators the precision can be very high while the ambiguity distance can be made large enough that any remaining ambiguity can be resolved by comparison with the RF measurements.

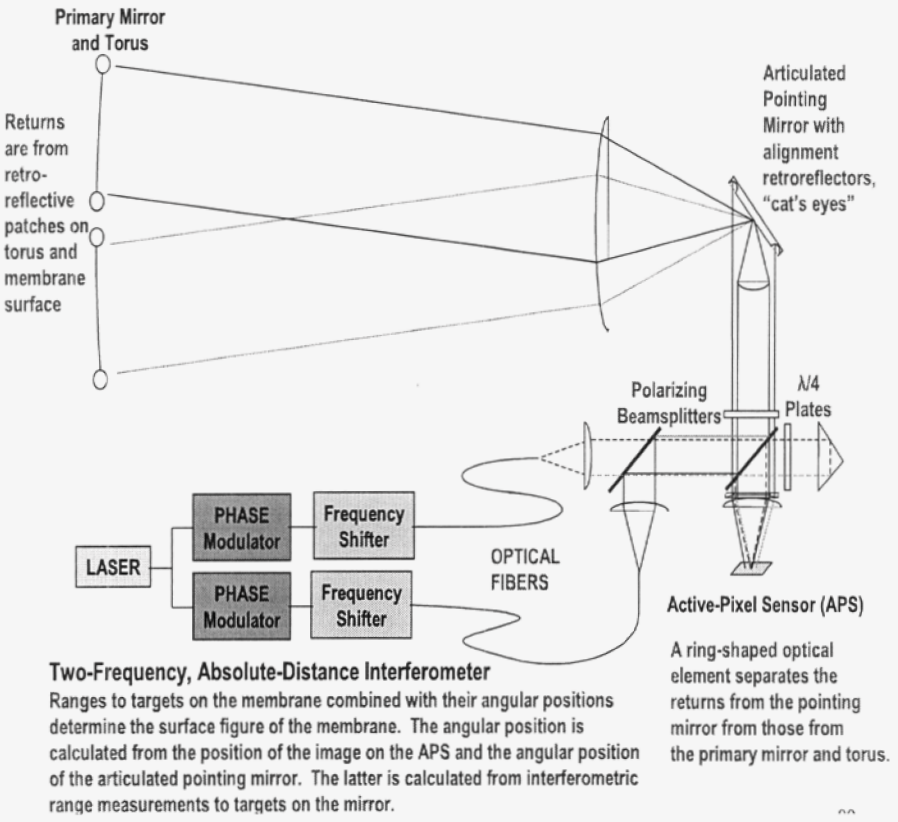

Figure 4: Surface-Figure metrology

3.5 Center-of-Curvature Sensor

In the deployment phase of the mission, using first the Formation RF sensor and then the Optical-Metrology sensor the positioning of the Science Spacecraft is refined until the Center-of-Curvature sensor can be activated, Figure 5. Then, center-of-Curvature sensor provides initial test of the quality of the spherical shape of the mirror.

Light from an optical fiber floods the surface of the primary mirror from a point adjacent to the center of curvature. A perfect mirror will return the light to a focus symmetrically located with respect to the center of curvature and will produce two uniformly illuminated out-of-focus spots on the two detectors. Deviations form the correct location, or the ideal surface figure are determined by a photometric analysis of the out-of-focus images.

4 Different Orbits Under Consideration

The first trajectory under consideration is defined by a point on Sun-Earth line which is 1.51 million km away from Earth. This is Sun-Earth L2 point [20] if the trajectory of Earth around Sun is assumed

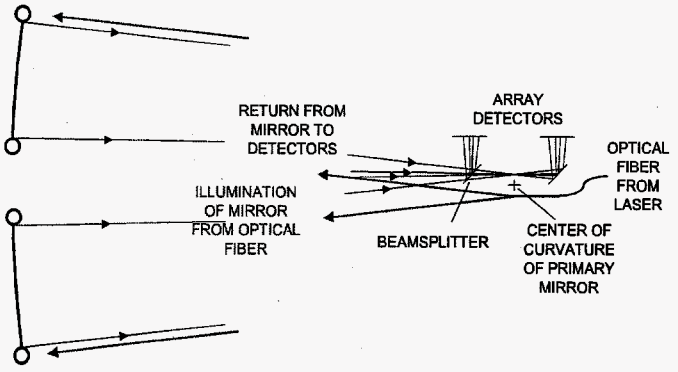

Figure 5: Center-of-Curvature Sensor

to be a perfect circle. Then, we consider the Sun-Earth L2 point with the actual orbit of Earth around Sun obtained either from a three body simulation of Sun-Earth-Moon system, or from prescribed orbits of Sun-Earth-Moon. A third orbit is also considered, which has the least severe ΔV requirement among the three. This orbit is constructed by projecting Sun-Barycenter L2 onto the Sun-Earth line (by Barycenter, we refer to the barycenter of the Earth-Moon system). The computation of Sun-Barycenter L2 point is done by lumping Earth-Moon mass onto Barycenter, which is located at the mass center of Sun and Moon. The reduction in ΔV requirements are observed to be significant (nearly half of the former ones), and this cylindrically constrained orbit also satisfies all science requirements. Therefore, we will refer to this orbit as the "optimal orbit on Sun-Earth line" for all practical purposes.

We name these orbits as Orbit-1,2, and 3 in the order mentioned above, i.e. Orbit-1 is the orbit with fixed distance from Earth, Orbit-2 is point at Sun-Earth L2 point, and Orbit-3 is the point at the projection of Sun-Barycenter L2 point on Sun-Earth line [1].

ΔV is computed by using 1 or 2-norm of the inertial acceleration vector of the orbit point, i.e.

$$\Delta V_{avg_{1,2}} = \frac{1}{N} \int_0^T \|\vec{a}_N(t)\|_{1,2} \, dt \,, \tag{1}$$

where, $\vec{a}_N$ is the net inertial acceleration, and N is the number of days in time period T. Then, we also computed ΔV requirements in radial, tangential, and normal directions. Radial direction is the direction from Earth to the point (which is same as the direction described by Sun-Earth line), and tangential and normal directions describe the plane normal to the radial direction. It is assumed that Earth-Moon orbit and Sun-Barycenter orbit are independent from each other, and they are solved by using two body formulations. The Sun-Barycenter and Earth-Moon orbits have prescribed eccentricities. Also, the Earth-Moon orbit around the Barycenter is assumed to have 5.15 degrees of inclination with respect to the plane described by the orbit of Barycenter around Sun. The numerical computations

[1] We would like to gratefully acknowledge Carlos Roithmayr, Spacecraft and Sensors Branch, NASA LaRC for his important observation of cylindrical constraint boundary to the orbit motions of the observatory.

Orbit	ΔV_{avg_2} $(m/s/day)$	ΔV_{avg_1} $(m/s/day)$	$\Delta V_{radial,avg}$	$\Delta V_{tangential,avg}$	$\Delta V_{normal,avg}$
1	2.95	3.91	1.94	1.81	0.16
2	2.93	3.88	1.90	1.82	0.16
3	1.63	1.96	0.24	1.56	0.16

Figure 6: Fuel Requirements for Different Orbits

Orbit	Max. Radial Force (mili-N)	Max. Tangential Force (μN)	Max. Normal Force (mili-N)
1	41.2	38.7	3.4
2	41.2	36.8	3.4
3	5.3	31.8	3.4

Figure 7: Thrust Requirements for Different Orbits

are performed for a time period of a year. The results are:

We also present the maximum specific force (force per kg of mass) components for each orbit:

The radial motion of the point tracked for Orbit-3 is given in Figure 8. It is computed that, 15% to 16.5% of the Sun can be observed from Orbit-3 (occultation of Sun is 84.5% to 85%). The variations of mean monthly distance of the orbit point to Earth is due to the eccentricity of the orbit of Barycenter around Sun.

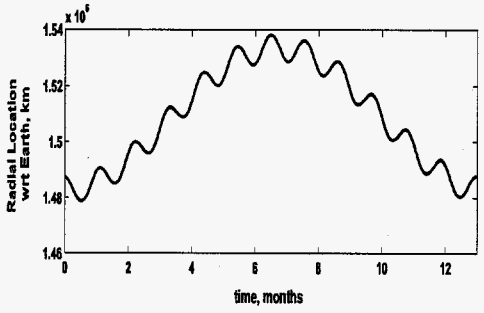

Figure 8: Motion of Orbit-3

5 Actuation

In this section, we discuss a thruster configuration which is duplicated on both spacecraft buses. We propose a propulsion scheme, and point out some imperfections that can arise during thrusting. We use thrusters for translational control, and reaction wheels for attitude control. Since disturbance torques are very small, we can consider the reaction wheels as linear actuators for our application.

5.1 Thruster Configuration and Sizing

We use two sets of thrusters for translation control, *large* and *small* thrusters. Large thrusters provide feed-forward control forces as well as orbital feedback forces in radial-tangential plane. Small thrusters provide formation control forces, provide orbital feed-forward and feedback forces in normal direction (which are an order smaller than radial and tangential components), and counteract residual forces in normal direction caused by large thruster firings (because of canted large thrusters).

We propose using electric propulsion (EP) with Xenon as the fuel. Current state of the art application for EP is the ion thrusters on NASA's Deep Space-1 spacecraft [3]. The current technology can produce high specific impulses (3500 secs for DS-1 thrusters). This makes EP the most attractive choice for our application, which should last 5-10 years without re-fueling. Therefore, we need high specific impulses which will reduce the fuel requirements. The current forecast suggest specific impulses (Isp) of 6000 secs for EP thrusters. This makes our mission feasible in terms of fuel requirements for a 5-10 years mission. One can observe this with a simple computation (which will also be substantiated with more complicated simulations), where we use the required ΔV values for Orbit-3. In Orbit-3, we have $\Delta V_{avg_1} = 1.96\ m/s/day$. If we assume ideal orthogonal thrusting, with $Isp = 6000$ secs, then we obtain a fuel requirement per unit mass of the payload for ten years as 0.1216 kg / kg-payload. This number gives a lower bound on the fuel requirement for a ten year mission, however, since the environmental disturbances are not substantial, we do not expect to deviate from this number significantly. Note that this corresponds to approximately 0.94×10^{-3} kg fuel per month (28 days), per kg of payload.

The thruster configuration and sizing can be performed by using the orbital properties of the mission. Since, we follow Orbit-3 (see Section 4 for a description of this orbit), we have to counteract forces which are on average significantly larger in tangential direction. Note that $\Delta V_{radial,avg} = 0.24$ (m/s/day), $\Delta V_{tangential,avg} = 1.56$ (m/s/day), and $\Delta V_{normal,avg} = 0.16$ (m/s/day) for this orbit, which is a measure of average accelerations to be provided for the orbit following. The peak values of thrust required in each direction per kg of payload are 5.3, 31.8 and 3.4 mN in radial, tangential, and normal directions. We propose a thruster configuration where there are four large thrusters on each face of the bus (faces which have normals to be aligned with the radial direction), canted so that their lines of action go through the nominal center of mass (CM) (which is currently assumed to be the geometric center), and, if necessary, they could have gimballing capabilities to account for any minor CM motion during the mission. This canting together with thruster locations provided significantly more actuation force in the tangential direction (nearly 83% of the thrust in tangential direction).

Currently, we propose to have 12 small thrusters in S/C-S, and 16 small ones in S/C-A. We present the thruster configurations in figures 9 and 10. Note that we only presented one figure (Figure 10) for S/C-A to avoid repetition, where the only difference is having 4 additional thrusters.

While sizing these thrusters, we use the peak force corresponding to a 1200 kg spacecraft. The most critical case is when all peaks occur simultaneously, and only one thruster is assigned to counteract these orbital forces. Then the thrust needed is 39 mN. Accounting for feedback forces (which are assumed to be a magnitude less than feed-forward forces), we require large thrusters with 45 mN or larger thrust capacity per kg of payload. The small thrusters are assumed to be providing forces for

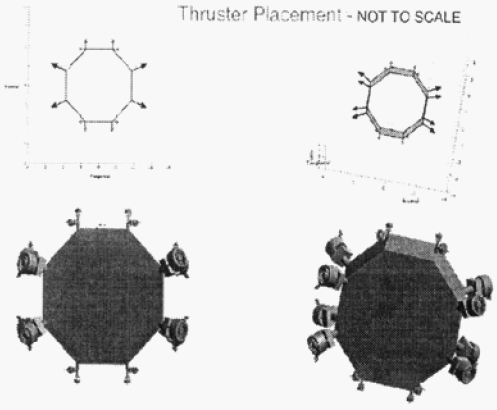

Figure 9: Thrusters

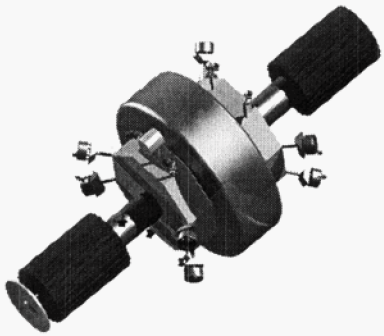

Figure 10: Thrusters on S/C-A, a predeployment configuration

formation control which counteracts differential disturbances between two spacecraft (mainly due to solar forces), so they are assumed to be providing forces of order 1-2 mN for these disturbances, as well as orbital feed-forward forces in normal direction and normal residuals from large thruster firings. Since our application has spacecraft with a mass about 1200 kg each, the normal residual forces and orbital feed-forward forces will be more critical. Therefore, we decided to use small thrusters with 5 mN peak thrust capacity per kg of payload.

Note that the number and configuration of thrusters allow us to accommodate some thruster failures. This is a desirable aspect of thruster configuration for a long duration deep space mission, where thrusters continuously fire.

6 Orbit Following and Formation Control

In this section, we describe a control strategy to keep the desired orbit and to establish fine formation control. We also describe a thruster configuration which is the same for both spacecraft, and simulate the behavior of the controller under imperfections in thrusters, as well as imperfections in the knowledge used by the controller.

A block diagram representation of sensing, estimation, and control is given in Figure 11. The spacecraft have two control modes, namely,

- Deployment mode,
- Formation mode.

In the *deployment mode*, both spacecraft have their own attitude and orbit controller, and sensor. This approach provides autonomy for each spacecraft during the deployment phase. Since the formation flying does not exist in this phase, they have to avoid collisions until the formation is established. In the *formation mode*, we have a central formation and orbit estimator, and controllers in the Science spacecraft producing the necessary control actions, which are then communicated to the other spacecraft. A detailed discussion of the formation mode control is given in this chapter.

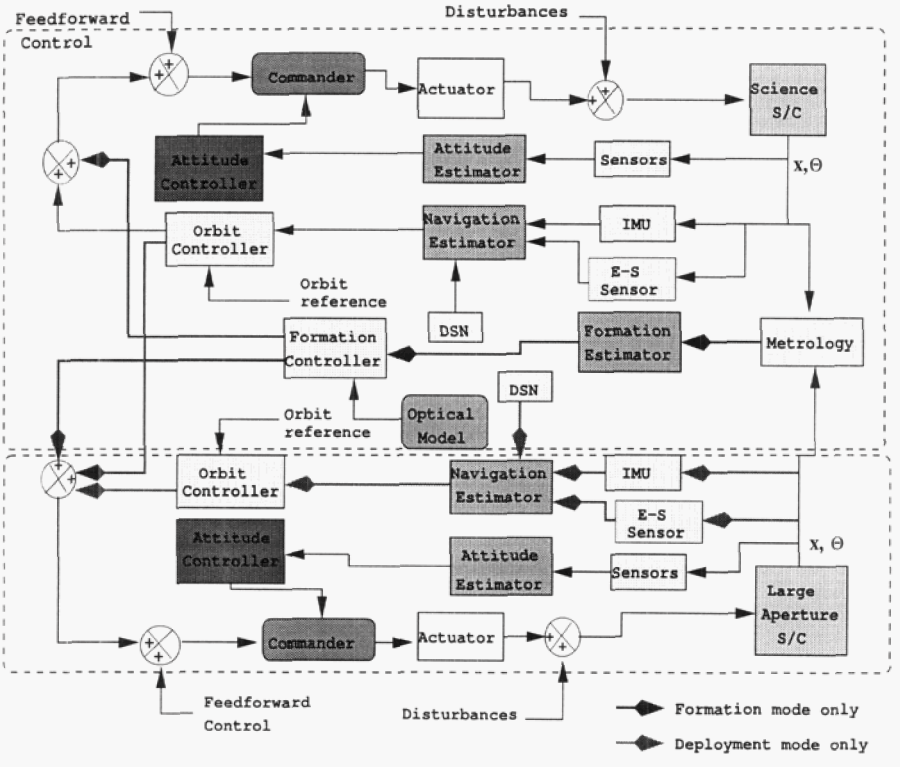

Figure 11: Estimation and Control

6.1 Translation Control Strategy

We have three major sets of control input,

- Feed-forward control input for mean orbit following, which is common to both spacecraft.
- Feedback control input for tracking the orbit to reject disturbances, which is common to both spacecraft.
- Feedback control for fine formation control, which can be different for each spacecraft.

The translational equations of motion for each spacecraft in a moving frame of reference with origin at the orbit point to be followed, and orientation aligned with radial, tangential and normal directions, are

$$\ddot{\vec{\rho}}_k = \sum \vec{f}_k - \ddot{\vec{r}}_p - 2\vec{\Omega} \times \dot{\vec{\rho}}_k - \dot{\vec{\Omega}} \times \vec{\rho}_k - \vec{\Omega} \times (\vec{\Omega} \times \vec{\rho}_k), \tag{2}$$

where, $k = 1, 2$, $\vec{\rho}_k$ is the position vector of kth spacecraft with respect to the orbit point, $\vec{\Omega}$ is the angular velocity vector of rotating frame with respect to the inertial frame, $\sum \vec{f}_k$ is the sum of all external acceleration vectors on kth spacecraft, and $\vec{r}_p$ is the position vector of the orbit point with respect to Sun. Here all vectors are expressed in the moving coordinate system, and the time derivatives are differentials with respect to the inertial frame. The external accelerations acting on each spacecraft can be expressed as

$$\sum \vec{f}_k = \vec{f}_{g_k} + \vec{u}_k + \vec{w}_k,$$

where $\vec{u}_k$ are control accelerations applied by thrusters, $\vec{w}_k$ are disturbance accelerations including solar forces, and $\vec{f}_{g_k}$ is the gravitational acceleration given by

$$\vec{f}_{g_k} = -G\left[\frac{m_S}{\|\vec{r}_k\|^3}\vec{r}_k + \frac{m_E}{\|\vec{r}_{kE}\|^3}\vec{r}_{kE} + \frac{m_M}{\|\vec{r}_{kM}\|^3}\vec{r}_{kM}\right],$$

where m_S, m_E, m_M are mass of Sun, Earth and Moon, $\vec{r}_k, \vec{r}_{kE}, \vec{r}_{kM}$ are the position vectors of kth spacecraft with respect to Sun, Earth and Moon, and G is the universal gravitational constant.

The main control objectives are:

- Keep the formation in the close neighborhood of the orbit point, i.e. the formation does not move out of a circle with center on Sun-Earth line and radius of 200 km, on the plane orthogonal to radial direction. Also, keep the radial distance from orbit point small enough so that the occultation of Sun is at reasonable (10-20 %) levels.
- Keep the formation aligned parallel to Sun-Earth line, with a distance of 125 m in between two spacecraft.

Now, we describe the dynamics of both spacecraft in a form that will be used in control design

$$m_k \ddot{y}_k = F_o + F_k + u_o + u_k + u_3 + w_k, \qquad k = 1, 2, \tag{3}$$

where y_k, $k = 1, 2$, are the position vectors of spacecraft with respect to the orbit point expressed in rotating frame, and

- F_o are known external forces, which contain gravitational forces, and forces caused by the acceleration of the orbit point, as well as some nominal value of solar pressures.
- F_k are the known orbital forces caused by the rotation of the moving frame (related with $\vec{\Omega}$), which are not used in feed-forward control, and treated as disturbances in feedback design.
- u_o is the feed-forward control force for tracking the orbit, which is common to both spacecraft.
- u_k, $k = 1, 2$, are the feedback control forces for each spacecraft, for formation control.
- u_3 is the feedback control force for orbit following, which is common to both spacecraft.
- w_k, $k = 1, 2$, are the uncertain disturbance forces on each spacecraft.

Note that, since $\vec{\Omega}$ has a very small magnitude and it varies extremely slowly in time, F_k can be treated like a very small magnitude disturbance to the system, rather than a nonlinearity in system's dynamics. Therefore, we will lump this term into disturbances in the rest of this report.

The choice of feed-forward control force is very straight forward, i.e.

$$u_o = -F_o\,. \tag{4}$$

With this choice of feed-forward control, we can describe the relative dynamics of two spacecraft, $\delta y = y_1 - y_2 - v_r$, where v_r is the desired constant relative position vector, and the dynamics of 2nd spacecraft as

$$\begin{aligned} \ddot{y}_2 &= \frac{1}{m_2}(u_2 + u_3 + w_2) \\ \delta\ddot{y} &= \frac{1}{m_1}(u_1 + w_1) - \frac{1}{m_2}(u_2 + w_2)\,. \end{aligned} \tag{5}$$

6.1.1 Formation Translation Control

Equations (5) show that the relative dynamics is decoupled from the overall dynamics. Therefore, we design a feedback controller for formation control independently. The controller will be a multi input-output PID controller (actually it is a multi-input single output control if we consider dynamics on each axis separately). In order to formulate the controller, lets write the relative dynamics in state space form,

$$\dot{x}_r = A_r x_r + B_r u_r + E_r w_r\,, \tag{6}$$

where, $x_r = (\delta y, \delta\dot{y})$, $u_r = (u_1, u_2)$, $w_r = w_1/m_1 - w_2/m_2$, and

$$A_r = \begin{pmatrix} 0 & I \\ 0 & 0 \end{pmatrix}, \quad B_r = \begin{pmatrix} 0 & 0 \\ I/m_1 & -I/m_2 \end{pmatrix}, \quad E_r = \begin{pmatrix} 0 \\ I \end{pmatrix}$$

Note that, we can assume that w_r is an almost constant disturbance signal. Then, we design a PID controller, by augmenting the system dynamics with the dynamics of integral of the error, i.e.

$$x_I \triangleq \int_0^t \delta y(\tau) d\tau\,.$$

Then the overall dynamics is given by

$$\dot{\xi}_r = \tilde{A}_r \xi + \tilde{B}_r u + \tilde{E}_r w,$$

where $\xi_r = (x_r, x_I)$, and letting $C = [I \;\; 0]$

$$\tilde{A}_r = \begin{pmatrix} A_r & 0 \\ C & 0 \end{pmatrix}, \quad \tilde{B}_r = \begin{pmatrix} B_r \\ 0 \end{pmatrix}, \quad \tilde{E}_r = \begin{pmatrix} E_r \\ 0 \end{pmatrix}.$$

Then, we choose a stabilizing gain matrix K by solving the following Riccati matrix equation,

$$P\tilde{A}_r + \tilde{A}_r^T P - P\tilde{B}_r \tilde{B}_r^T P + Q = 0,$$

where $Q = Q^T > 0$ is a positive definite matrix of appropriate dimensions, and P is the matrix variable solved for. Note that, when the pair (A_r, B_r) is stabilizable, and the following rank condition holds

$$Rank \begin{pmatrix} A_r & B_r \\ C & 0 \end{pmatrix} = 6,$$

the Riccati equation given above has a positive definite solution for P (see [2, 6]). In our case, these assumptions are satisfied. Therefore, we can compute the stabilizing gain matrix by using

$$K = -k\tilde{B}_r^T P, \quad \text{where } k \geq 1.$$

Then we can choose the following feedback control law that establishes the accurate relative position of two spacecraft [1, 2],

$$u = \begin{pmatrix} u_1 \\ u_2 \end{pmatrix} = K_P \delta y + K_D \delta \dot{y} + K_I \int_0^t \delta y(\tau) d\tau,$$

where

$$K = [\, K_P \;\; K_D \;\; K_I \,].$$

6.1.2 Orbit Feedback Control

Since we expect very large measurement errors for relative position with respect to the orbital point to be followed, we design a feedback closed loop system with much smaller bandwidth for orbit feedback control. We use a similar approach in designing orbital feedback control as in formation control. Before designing the orbital feedback control, note that the closed loop formation dynamics is decoupled from orbital dynamics (5), and it is stable. Because of this upper triangular and linear dynamics, designing a linear stabilizing controller independently for orbit following is sufficient to have the overall stability of the formation and orbit following.

First, define the following dynamics from (5)

$$\ddot{y}_2 = \frac{1}{m_2} u_3 + d$$

where $d = (u_2 + w_2)/m_2$, which is treated as almost constant disturbance. We use a PID controller in this case, so the equation above becomes

$$\dot{v} = \frac{1}{m}\left(K_P y_2 + K_D v + K_I \int_0^t y_2(\tau)d\tau\right) + d,$$

for some K_P, K_D and K_I, where $v \triangleq \dot{y}_2$. Now, since we like to distinguish the time, length and velocity scales of orbital control (because of large measurement errors as well as very slow response times), we will describe the following scaled variables

$$\tilde{t} = \frac{t}{T}, \quad \tilde{y} = \frac{y_2}{L}, \quad \tilde{v} = \frac{v}{U},$$

where $T >> 1$, $L >> 1$, $U > 1$ are relevant time, length, and velocity scales. For example, T can be in the order of days, and L can be in the order of tens of kilometers. Then, we can write the equations above as

$$\tilde{v}' = \frac{1}{m_2}\left(\frac{LTK_P}{U}\tilde{y} + TK_D\tilde{v} + \frac{LT^2K_I}{U}\int_0^{\tilde{t}} \tilde{y}(s)ds,\right) + \tilde{d}$$

where

$$(\cdot)' \triangleq \frac{d(\cdot)}{d\tilde{t}}, \quad \text{and} \quad \tilde{d} = \frac{Td}{U}.$$

We define

$$\tilde{K}_P = \frac{LTK_P}{U}, \quad \tilde{K}_D = TK_D, \quad \tilde{K}_I = \frac{LT^2K_I}{U}, \tag{7}$$

then we obtain

$$\tilde{v}' = \frac{1}{m_2}\left(\tilde{K}_P\tilde{y} + \tilde{K}_D\tilde{v} + \tilde{K}_I\int_0^{\tilde{t}} \tilde{y}(s)ds\right) + \tilde{d}.$$

This equation can be expressed in a state space form as

$$\dot{\tilde{\xi}} = \tilde{A}\tilde{\xi} + \tilde{B}\tilde{u} + \tilde{E}\tilde{d}$$

where

$$\tilde{\xi} = \begin{pmatrix} \tilde{y} \\ \tilde{v} \\ \tilde{x}_I \end{pmatrix}, \quad \tilde{u} = [\,\tilde{K}_P \;\; \tilde{K}_D \;\; \tilde{K}_I\,]\tilde{\xi}, \quad \tilde{x}_I = \int_0^{\tilde{t}} \tilde{y}(s)ds,$$

and

$$\tilde{A} = \begin{pmatrix} 0 & I & 0 \\ 0 & 0 & 0 \\ I & 0 & 0 \end{pmatrix}, \quad \tilde{B} = \begin{pmatrix} 0 \\ I \\ 0 \end{pmatrix}, \quad \tilde{E} = \begin{pmatrix} 0 \\ I \\ 0 \end{pmatrix}.$$

Then, we can design the gain matrix $\tilde{K} = [\,\tilde{K}_P \;\; \tilde{K}_D \;\; \tilde{K}_I\,]$ by solving for

$$P\tilde{A} + \tilde{A}^T P - P\tilde{B}\tilde{B}^T P + Q = 0$$

where $Q = Q^T > 0$ is some positive definite matrix, and

$$\tilde{K} = -k\tilde{B}^T P, \quad \text{where } k \geq 1.$$

Once the components of $\tilde{K}$ are computed, then we can find K_P, K_D, K_I by using relations given in (7). Note, that this design procedure can be applied in a decoupled way to all axes, and the scaling parameters T, L and U can be chosen differently for different axes.

MT = 20%, TI = 0.2 mN and 1.6 mN	S/C-A	S/C-S		
Fuel (kg/month)	1.25	1.24	Max. Formation Error (mm)	14
			Max. Tangential Orbit Error (km)	30
Fuel for Large Thrusters (kg/month)	0.98	0.98	Max. Normal Orbit Error (km)	35
Fuel for Small Thrusters (kg/month)	0.27	0.26	e_t, e_n km	30, 30
Max. Total Thrust (mN)	57.6	57.6	e_{fr}, e_{ft}, e_{fn} mm	0.5, 0.7, 0.7

MT: Minimum thrust level with respect as a percentage of Maximum Thrust
TI: Thrust increments in small and large thrusters

Figure 12: Results with Course Thrusting

7 Simulation Results

In this section, we present simulation results in order to compute fuel requirements under more realistic conditions, as well as system response to imperfections in actuation and sensing. We assume that both spacecraft are 1000 kg each, with the thruster configuration explained earlier (note that 1000 kg spacecraft implies that large thrusters have peak capacity of 40 mN and small ones have 5 mN). The minimum thrust level are assumed to be 20 % and 5 % of the maximum thrust, with a quantization of 20 and 40 thrust levels. We simulate some sensor measurement errors by adding zero mean Gaussian white noise on the states, and then state estimation is done by implementing linear Kalman filters [10]. The standard deviation of

The first set of results are obtained from a simulation of 28 days, with 20% minimum thrust levels (8 mN for large, 1 mN for small thrusters). The results show that the formation errors are ± 1.4 cm, and orbit following is achieved with a reasonable accuracy. The results are summarized in the following table:

where e_t, e_n are standard deviations of zero mean Gaussian measurement errors for distances from the desired orbit in tangential, and normal directions, and e_{fr}, e_{ft}, e_{fn} are corresponding values for relative position measurement errors in radial, tangential, and and normal directions. These values come from experiences obtained from previous missions, and from some geometrical arguments, so they are rough estimates of the measurement error characteristics. Some simulation results are given in Figures 13 and 14.

The second set of results are obtained from a simulation of 28 days, with 5% minimum thrust levels (2 mN for large, 0.25 mN for small thrusters). The results show that the formation errors are ± 2.8 mm, and orbit following is achieved with a reasonable accuracy. The results are summarized in the following table:

Some simulation results are given in Figures 16 and 17. Note that formation keeping errors are significantly lower than the ones with course thrusting, 14 mm versus 2.8 mm, and also max total thrust levels are lower about 8 mN. The formation keeping errors in the case of course thrusting is close to our formation error budget of 2 cm. These results suggest that thrusters with finer thrust levels and lower minimum thrust levels can improve the formation performance significantly.

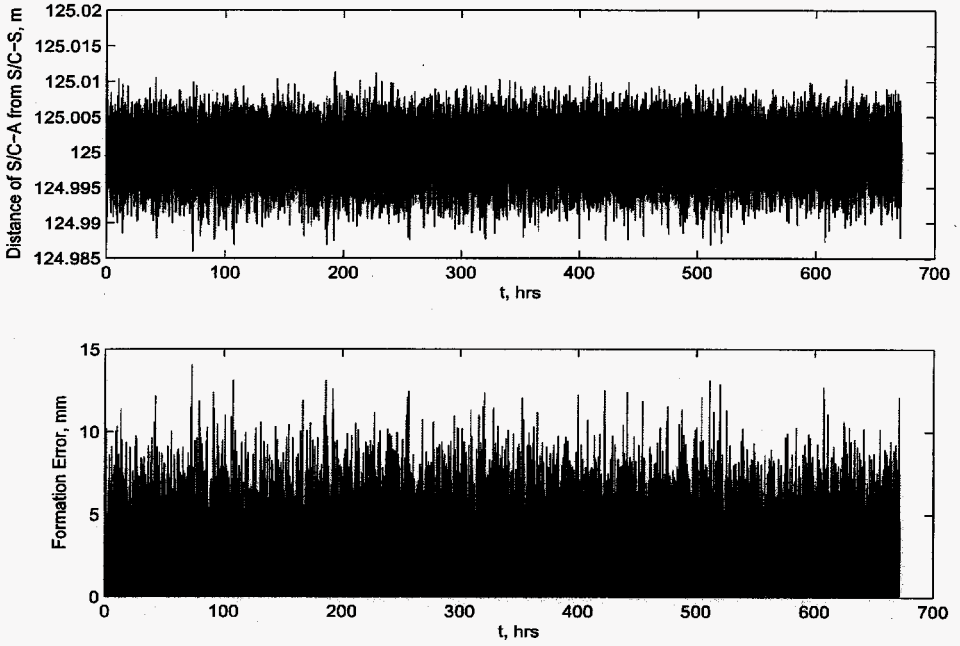

Figure 13: Simulation, Course Thrusting

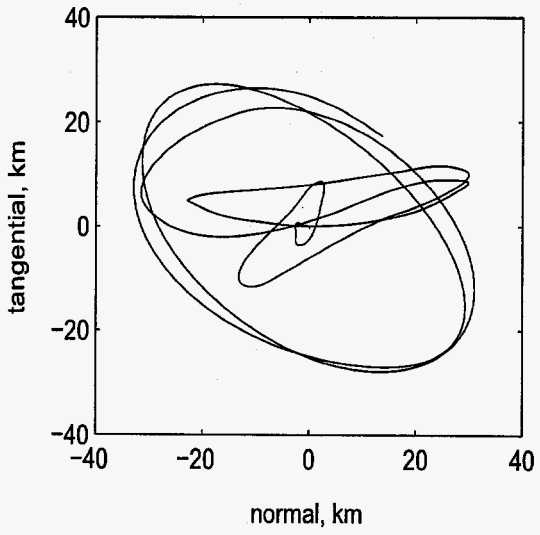

Figure 14: Simulation, Course Thrusting

MT = 5%, TI = 0.1 mN and 0.8 mN	S/C-A	S/C-S		
Fuel (kg/month)	1.22	1.21	Max. Formation Error (mm)	2.8
			Max. Tangential Orbit Error (km)	15
Fuel for Large Thrusters (kg/month)	0.98	0.98	Max. Normal Orbit Error (km)	25
Fuel for Small Thrusters (kg/month)	0.24	0.23	e_t, e_n km	30, 30
Max. Total Thrust (mN)	50.3	49.9	e_{fr}, e_{ft}, e_{fn} mm	0.5, 0.7, 0.7

MT: Minimum thrust level with respect as a percentage of Maximum Thrust
TI: Thrust increments in small and large thrusters

Figure 15: Results with Fine Thrusting

8 Primary Mirror Shape Control

In this part of the report, we discuss possible control techniques for shape control of the 25 meter primary mirror. The mass of the mirror is the most important design parameter that motivates the development of new design concepts and technologies. Development of large, ultra-light weight space telescopes is also one of the primary technology focus areas of NASA. The proposed mirror in our application has a surface area about 450 m^2. We baseline our design in order to have a mass about 1200 kg for the Large Aperture Spacecraft, which contains the mirror, the supporting structure (inflatable torus), and the engineering bus. This implies that we must have a mirror of areal density less than 1 kg/m^2 [14, 24]. The current lightweight glass-based mirrors have areal densities of $15-20$ kg/m^2. Foam and SiC technologies are shown to bring this number down to $10kg/m^2$ levels, but this is still extremely heavy and unacceptable for our application. This motivates usage of ultra-light membrane type flexible mirrors. The wavefront abberations can be corrected by adaptive optics in a corrector mirror in the Science spacecraft [8, 21]. However, there is no available wave front sensor technology to detect the abberations caused by the large mirror. Therefore, we propose a fine shape control of the spherical large mirror, and correction of only the spherical abberations by the corrector mirror.

8.1 A Shape Control Strategy for the Membrane Mirror

We consider a combined approach of depositing an optical quality reflecting surface onto a Nitinol shape memory alloy (SMA) 5 micron thick membrane that has been preconditioned to deploy to a nominally spherical shape. Two layers of 10 micron orthogonally polarized piezoelectric membranes are bounded behind the SMA. The desired deformations to control the spherical shape are obtained by applying voltage distributions through a unique pattern of sparsely deposited electrodes that locally contract or expand the piezo-material to cause bimorph actuation (biaxial bending) for precision shape control. We carry out a fine wavefront control of the large membrane as a Schmidt mirror, and leave only residual spherical abberations corrected by a small adaptive Schmidt corrector optics in the receiver telescope on the secondary spacecraft.

The mirror, in our application, is supported by an inflatable torus in the inner and outer rim. The mirror geometry and the shape control concept are shown in Figure 18. The connection of the inner and outer torus to the mirror is accomplished by an *interface* region which is composed of PVDF strips

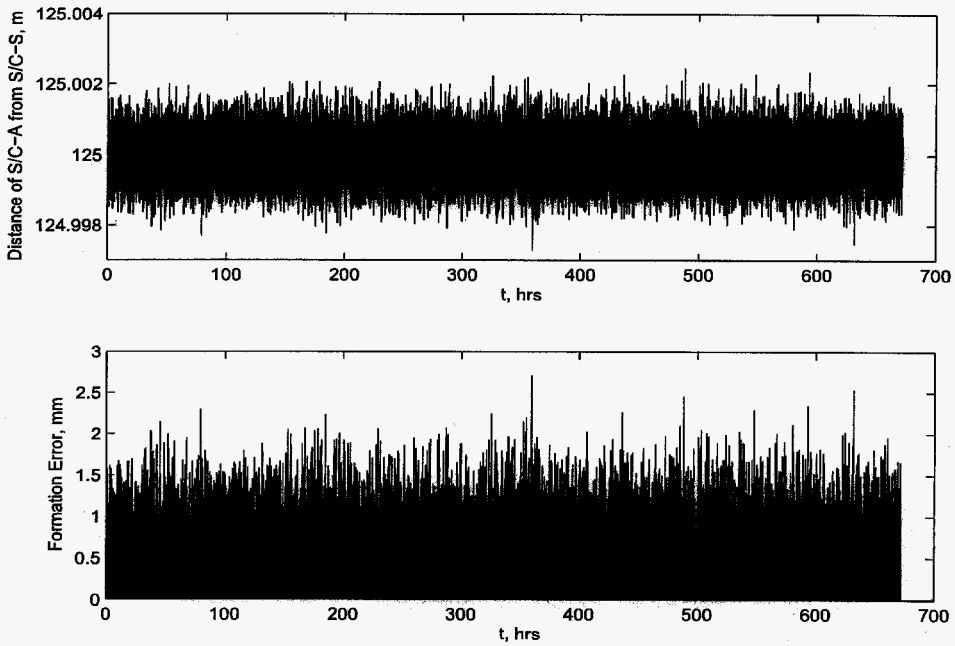

Figure 16: Simulation, Fine Thrusting

connecting the mirror to the torus. PVDF is used because of its low modulus of elasticity. Their back surface can have MEMS inchworm actuators [14] (which are capable of large strokes of about 250 microns), and they are connected to the torus via a large stroke piezo actuator. Therefore, the PVDF connector strips can be controlled such that the internal forces and moments at the joints with the mirror are minimized. By minimizing these reaction forces and moments, a soft connection between the mirror and the torus is established that prevents the transfer of any external forces from the torus to the mirror.

The control forces and torques for shape control are generated by applying a voltage to expand or contract bonded piezoelectric actuators. Some choices for piezoelectric materials for our application are PVDF (polyvinylidene fluoride), PZT, Polyurethane, which have different mass, strength, and thermal properties.

Based on the brief discussion above, our assessment is that, fine control of the nominal shape of the large mirror via SMA structure together with piezo actuation can achieve the desired optical performance. The following is a brief list of potential challenges in our baseline design, and possible improvements and alternatives that need further research:

- Manufacturing the optical quality membrane material desired for the large reflector surface.
- Developing a sensor technology, in terms of hardware and estimation software, to precisely measure the mirror surface, and estimate the deformations.
- Analyzing and mitigating the shape errors caused by differences thermal properties, i.e. different coefficient of thermal expansions for bonded surfaces.

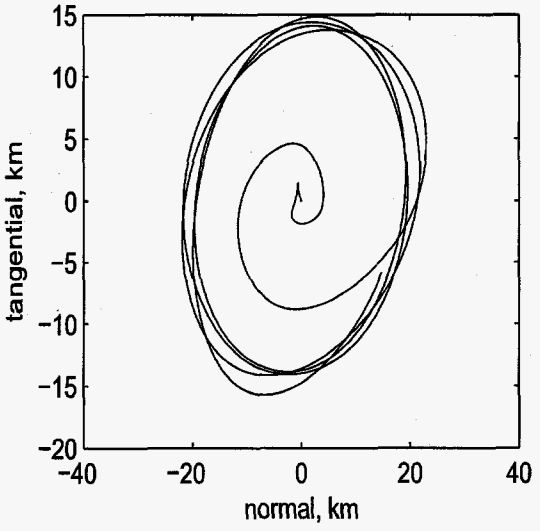

Figure 17: Simulation, Fine Thrusting

- Development of models describing the dynamics of the membrane together with the actuation [19].
- Development of efficient control algorithms, which can establish shape control to desired accuracies, with realizable actuation [25].
- Development of a wavefront sensor technology for the adaptive optics in the corrector mirror.

The modelling of the dynamics and control of the large mirror has two major steps, (see [15, 18, 19, 8, 7] for modelling of membranes, and piezoelectric actuators):

- Modelling the response of the piezoelectric material to the electrical excitation [22, 23].
- Modelling of nonlinear dynamics of thin shell mirror (mirror at its nominal spherical shape) together with the dynamics of piezoelectric material.

We propose a quasi-static modal control approach for the large mirror shape control. In this approach, the shape of the mirror is given in terms of orthonormal polynomials defined on a unit disk, which are known as Zernike polynomials [21]. Then, an algorithm that computes the required actuation will adjust the coefficients in these series in order to establish the desired spherical mirror shape.

In this approach the shape of the mirror is given in terms of orthonormal polynomials defined on a unit disk. Basically, we represent the shape function in terms of Zernike series, which have the desirable property of being orthonormal, i.e. the coefficient of each base function is independent of the coefficients of the other base functions. Then, our approach is to adjust the coefficients in these series in order to establish the desired mirror shape, which is spherical.

The general two dimensional Zernike series [21] is given in the following form:

$$z(\rho,\theta) = A_{00} + \frac{1}{\sqrt{2}} \sum_{n=2}^{\infty} A_{n0} R_n^0\left(\frac{\rho}{R}\right) + \sum_{n=1}^{\infty} \sum_{m=1}^{n} \{A_{nm}\cos m\theta + B_{nm}\sin m\theta\} R_n^m\left(\frac{\rho}{R}\right), \qquad (8)$$

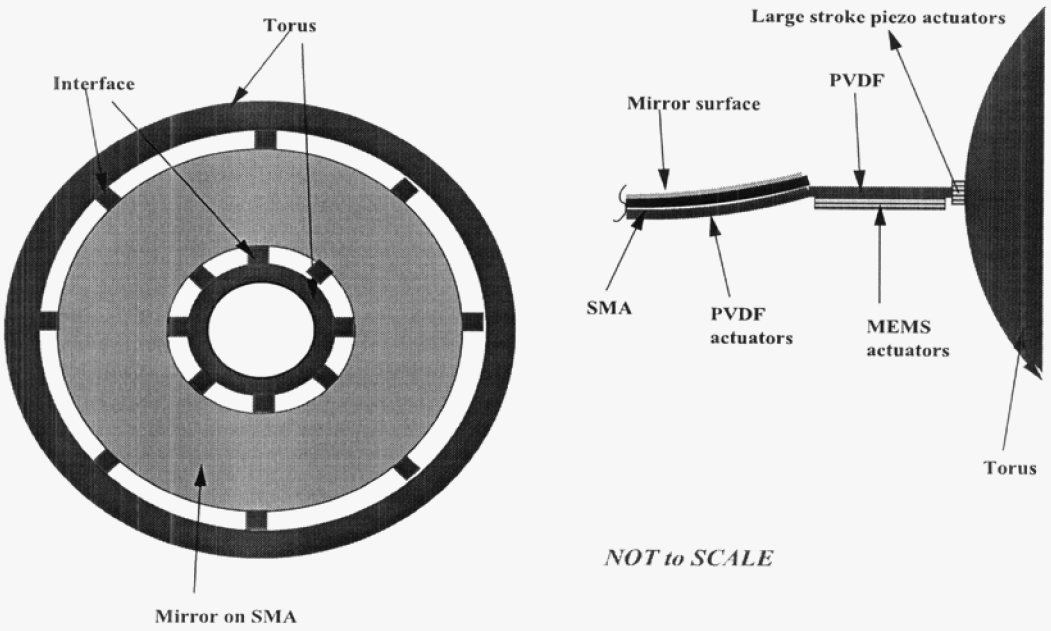

Figure 18: A Shape Control Strategy

where z represents the surface elevations, R is the radius over which the polynomials are defined, ρ, θ are the polar coordinates defined on the mirror plane, $n-m$ is even with R_n^m defined as

$$R_n^{\pm m}(\frac{\rho}{R}) = \sum_{k=0}^{\frac{n-m}{2}} (-1)^k \frac{(n-k)!}{k!(\frac{n+m}{2}-k)!(\frac{n-m}{2}-k)!} \left[\frac{\rho}{R}\right]^{n-2k},$$

and A_{nm} are Zernike coefficients. Zernike series have orthonormal terms over a circle, therefore they can effectively serve as a basis to any bounded piecewise continuous function defined on a circle. Consequently, surface deformations for the mirror can be effectively described by using these polynomials, and there are techniques available to extract the coefficients of these polynomials from sensed information. Our approach is to define a desired shape and then describe the deviation from this shape in terms of Zernike series, and adjust the Zernike coefficients with control actuation.

At L2 point of Sun and Earth, the large mirror will be exposed to disturbance forces which vary extremely slowly, such as solar pressure. Therefore, we can treat the shape control of large mirror as finding control forces to correct the static deformations at a given instant. The dynamics of the mirror is ignored in this approach, so the approach is static in nature. But, since this correction is done quite frequently and piezo actuation can be applied very rapidly, this can prove to be a reasonable simplification.

From this point on, each step in the control procedure is described in a generic mathematical form, in order to convey the ideas clearly.

The first step in our approach is to determine the shape of the mirror from the laser metrology measurements of the surface. Basically, given any surface shape at any instant, identify what are the

Zernike series coefficients that describe the mirror shape, i.e.

$$z(\rho,\theta)=\sum_{k=1}^{m} c_k Z_k(\rho,\theta),$$

where c_k, $k=1,\ldots,m$, are Zernike polynomial coefficients to be determined, m is the number of Zernike coefficients considered, and Z_k represents (in a compact way) the k th Zernike polynomial. After the measurements are performed, we have a set of data points $\{(\theta_i,r_j)\}_{i,j=1}^{n_i,n_j}$, and associated values of the quantity $\{z_{i,j}\}_{i,j=1}^{n_i,n_j}$, where $n_i \times n_j$ is the total number of measurement points. Now, the Zernike coefficients, $\{c_k\}_{k=1}^{m}$, have to be estimated. The main problem is having the possibility of measurement noise, and the estimation of these coefficients from such a noisy data. There are two major research problems that have to be studied:

- Statistical characterization of the sensor noise, such as being white, colored, stationary, non-stationary noise etc...
- Reliable computational algorithms to obtain the best estimate of the Zernike coefficients from the measured data, since accuracy of the estimation will be extremely critical to our control performance.

Significant amount of research and development has been recorded in the literature in *sinusoid estimation* from a noise corrupted data [4, 9, 11, 16] (and many other references). The main objective of that research is to estimate the components of some given orthonormal basis functions, that describes the functional form of a noise corrupted data. This is the basic objective, with a specific set of orthonormal functions, which are described on a unit circle (also see [12, 13] for a discussion on orthogonal polynomials). Therefore, research on estimation of Zernike polynomials from a noisy data is critical, and should be a priority.

Zernike coefficients contain two main components, i.e.

$$c_k = c_{k,0} + c_{k,c}, \qquad k=1,\ldots,m,$$

where $c_{k,0}$ is the k th Zernike coefficient representing initial surface shape errors in the mirror, and $c_{k,c}$ is the k th coefficient representing the surface shape response due to the applied control action. In order to find the required control action, we need to describe the effects of the voltages, applied on individual actuation patches, on Zernike coefficients, i.e. we have to establish a relation of the following form:

$$c_{k,c} = g_k(V_1,V_2,\ldots,V_n),$$

where $V_1,\ldots,V_n$ are the voltages applied on the patches, g_k is the function describing the influence of these voltages on Zernike coefficient $c_{k,c}$. These functions, g_k, $k=1,\ldots,n$, can directly be derived by using *influence functions* (see for example [21, 25, 5]), which establish relationship between applied voltage field and the resulting deformations, and which are functions of material properties of the mirror (modulus of elasticity, thickness, Poisson's ratio), and the boundary conditions that exist at the mirror edges, inner and outer edges in our application (and the initial nominal shape of the

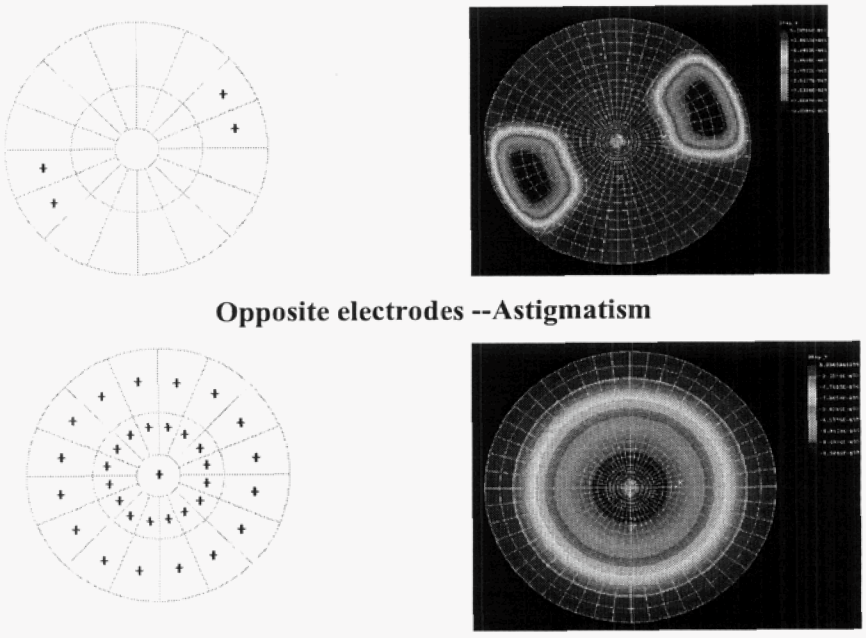

Figure 19: An example of numerical visualization of Influence Functions

mirror determined by the shape memory alloy particular to our approach). An example of numerical visualization of such influence functions is given in Figure 19, (this example is from [15] [2]).

As an example, suppose the functional relation describing influence of the voltages on Zernike coefficients is linear, and it is described by a matrix A, i.e.

$$c_c = \begin{pmatrix} c_{1,c} \\ c_{2,c} \\ \vdots \\ c_{m,c} \end{pmatrix} = A \begin{pmatrix} V_1 \\ V_2 \\ \vdots \\ V_m \end{pmatrix}.$$

Now, if the desired shape of the mirror (spherical in our case) is described by $\hat{z}(\theta,\rho) = \sum_{k=1}^{m} \hat{c}_k Z_k(\theta,\rho)$, we can find the necessary actuation to assume the ideal nominal shape by using a least squares (or minimum energy) described as following

$$\begin{pmatrix} V_1 \\ V_2 \\ \vdots \\ V_m \end{pmatrix} = (A^T A)^{-1} A^T \begin{pmatrix} \hat{c}_1 - c_{1,0} \\ \hat{c}_2 - c_{2,0} \\ \vdots \\ \hat{c}_m - c_{m,0} \end{pmatrix} \quad \left(\text{or} \quad = A^T (AA^T)^{-1} \begin{pmatrix} \hat{c}_1 - c_{1,0} \\ \hat{c}_2 - c_{2,0} \\ \vdots \\ \hat{c}_m - c_{m,0} \end{pmatrix} \right).$$

[2] We wish to gratefully acknowledge S. S. Lih of JPL for giving us the permission to use these figures.

Once the actuation voltages are determined, then they are applied to correct the deformations in order to attain as ideal shape as possible.

9 Conclusions

The results of this concept definition study show that the telescope concept is feasible, and can have technology readiness in the 2020 time frame. Further advanced developments in several subsystems are needed, such as higher efficiency Xenon ion thrusters with throttling, and optical quality large membrane mirror with active shape control.

Ion electric propulsion is a critical area for further research. Currently available ion thrusters with a specific impulse of 3000 sec have excessive fuel requirements for this mission. Therefore, development of more efficient ion thrusters with 6000 sec or more specific impulse is required for this mission. Furthermore, ion thrusters with finer throttle levels, and faster response to changes requested in throttle levels are also essential for high precision formation control.

Large membrane mirror shape control is another critical area of further advanced development. Production of such a large membrane mirror, deployment of it in space, and its shape control involve a wealth of engineering research problems. In this paper, we identify and discuss several key problems related to shape control that involve development of sensors, estimation algorithms, actuators, and control algorithms.

Acknowledgement

This research was performed at the Jet Propulsion Laboratory, California Institute of Technology, under the contract with National Aeronautics and Space Administration. This paper was supported by the NASA RASC (Revolutionary Aerospace Systems Concepts) program. We wish to gratefully acknowledge the membrane modeling advice of Drs. S. S. Lih, E. H. Yang, and M. B. Quadrelli of JPL, and J. Pellicciotti and C. Strickland of LaRC for structures and material technology advice. We also gratefully acknowledge J. Antol of NASA LaRC for his RASC program support, R. Manvi and C. Weisbin of JPL for their task coordination and integration efforts.

References

[1] A. B. Açıkmeşe and M. Corless. Robust constant output tracking for uncertain/nonlinear systems with PI controllers. *American Control Conference*, 2001.

[2] A. B. Açıkmeşe and M. Corless. Robust output tracking for uncertain/nonlinear systems subject to almost constant disturbances. *Automatica*, 38(11), 2002.

[3] J. R. Brophy, R. Y. Kakuda, J.E. Polk, J.R. Anderson, M. Marcucci, D. Brinza, M.D. Henry, K. Fujii, K.R. Mantha, J.F. Stocky, J. Sovey, M. Peterson, V Rawley, J. Hamley, T. Bond, J. Christensen, H. Cardwell, G. Benson, J. Gallagher, M. Matranga, and D. Bushway. *Ion Propulsion System (NSTAR) DS-1 Technology Validation Report, NASA Jet Propulsion Laboratory.*

[4] J. Capon. High-resolution frequence-wave number spectrum analysis. *Proceedings of IEEE*, 57, 1969.

[5] A. Chellabi, Y. Stepanenko, and S. Dost. A new control algorithm for bimorph mirrors. *IEEE International Conference on Systems, Man and Cybernetics*, 1, 1995.

[6] M. Corless and A. E. Frazho. *Linear Systems and Control: An Operator Perspective*. Marcel Dekker, 2003.

[7] E. M. Ellis. *IEEE Standard on Piezoelectricity, ANSI/IEEE Standard 176-1987*. IEEE, 1987.

[8] E. M. Ellis. *Low-Cost Bimorph Mirrors in Adaptive Optics*. Thesis, Imperial College of Science, Technology, and Medicine, University of London, 1999.

[9] A. E. Frazho and P. J. Sherman. On minimum variance spectrum estimator in nonstationary noise. *IEEE Transactions in Information Theory*, 37(5), 1991.

[10] A. Gelb. *Applied Optimal Estimation*. The M.I.T. Press, 1974.

[11] T. T. Georgiou. Spectral estimation via selective harmonic amplification. *IEEE Transactions in Automatic Control*, 46, 2001.

[12] L. Y. Geronimus. Polynomials orthogonal on a circle and their application. *Zapiski Nauchno-issledovatel'skogo in-ta Matematiki i Mekhaniki i KhMo*, 19, 1948.

[13] L. Y. Geronimus. Orthogonal polynomials. *Consultants Bureau, New York*, 1961.

[14] S. N. Gullapali, R. Flood, E. H. Yang, and S. S. Lih. New technologies for the actuation and control of large aperture lightweight optical quality mirrors. *IEEE*, 2003.

[15] G. S. Hickey, S. S. Lih, and T. Barbee. Development of nanolaminate thin shell mirror. *JPL Internal Communication*, 2003.

[16] T. Kailath. *Lectures on Linear Least-Squares Estimation, CISM Courses and Lectures*. Springer-Verlag, 1978.

[17] O. P. Lay, S. Dubovitsky, R. D. Peters, J. P. Burger, S.-W. Ahn, W. H. Steiner, H. R. Fetterman, and Y. Chang. Mstar: A submicrometer absolute metrology system. *Optics Letters*, 28(11), 2003.

[18] S. S. Lih, G. S. Hickey, J. H. Ding, and S. H. Tzou. Micro-control actions of segmented actuators on shallow paraboloidal shell reflectors. *ASME International Adaptive Structures and Materials Systems Symposium*, 2002.

[19] M. Quadrelli and S. Sirlin. Modeling and control of membranes for gossamer spacecraft. part 1: Theory. *42nd AIAA/ASME/ASCE/AHS/ASC Structures, Structural Dynamics, and Materials Conference*, 2001.

[20] A. E. Roy. *Orbital Motion, 3rd Edition.* University of Physics Publishing, 1988.

[21] R. Tyson. *Principles of Adaptive Optics.* Academic Press, 1997.

[22] H.S. Tzou and R. V. Howard. A piezothermoelastic thin shell theory applied to active structures. *ASME Transactions, Journal of Vibration and Acoustics*, 116:295–302, 1994.

[23] H.S. Tzou and R. Ye. Piezothermoelasticity and precision control of piezoelectric systems: Theory and finite element analysis. *ASME Transactions, Journal of Vibration and Acoustics*, 116:489–495, 1994.

[24] E. H. Yang, K. Schheglov, and S. Trolier-McKinstry. Concept, modelling and fabrication for large-stroke piezoelectric unimorph deformable mirrors. 2003.

[25] L. Zhu, P.C. Sun, D. U. Bartsch, W. R. Freeman, and Y. Fainman. Adaptive control of a micromachined continuous-membrane deformable mirror for abberation compensation. *Applied Optics*, 38(1).